nanomaterials

MDPI

Article

Nitrogen-Doped Reduced Graphene Oxide Supported $Pd_{4.7}Ru$ Nanoparticles Electrocatalyst for Oxygen Reduction Reaction

Gil-Ryeong Park [1], Seung Geun Jo [1], Anuraj Varyambath [1], Jeonghyun Kim [2,*] and Jung Woo Lee [1,*]

[1] Department of Materials Science and Engineering, Pusan National University, Busan 46241, Korea; rlffud1479@pusan.ac.kr (G.-R.P.); linkroot1128@pusan.ac.kr (S.G.J.); anurajvaryambath@gmail.com (A.V.)
[2] Department of Electronic Convergence Engineering, Kwangwoon University, Seoul 01899, Korea
* Correspondence: jkim@kw.ac.kr (J.K.); jungwoolee@pusan.ac.kr (J.W.L.); Tel.: +82-51-510-2898 (J.W.L.)

Abstract: It is imperative to design an inexpensive, active, and durable electrocatalyst in oxygen reduction reaction (ORR) to replace carbon black supported Pt (Pt/CB). In this work, we synthesized $Pd_{4.7}Ru$ nanoparticles on nitrogen-doped reduced graphene oxide ($Pd_{4.7}Ru$ NPs/NrGO) by a facile microwave-assisted method. Nitrogen atoms were introduced into the graphene by thermal reduction with NH_3 gas and several nitrogen atoms, such as pyrrolic, graphitic, and pyridinic N, found by X-ray photoelectron spectroscopy. Pyridinic nitrogen atoms acted as efficient particle anchoring sites, making strong bonding with $Pd_{4.7}Ru$ NPs. Additionally, carbon atoms bonding with pyridinic N facilitated the adsorption of O_2 as Lewis bases. The uniformly distributed ~2.4 nm of $Pd_{4.7}Ru$ NPs on the NrGO was confirmed by transmission electron microscopy. The optimal composition between Pd and Ru is 4.7:1, reaching -6.33 mA/cm^2 at 0.3 V_{RHE} for the best ORR activity among all measured catalysts. Furthermore, accelerated degradation test by electrochemical measurements proved its high durability, maintaining its initial current density up to 98.3% at 0.3 V_{RHE} and 93.7% at 0.75 V_{RHE}, whereas other catalysts remained below 90% at all potentials. These outcomes are considered that the doped nitrogen atoms bond with the NPs stably, and their electron-rich states facilitate the interaction with the reactants on the surface. In conclusion, the catalyst can be applied to the fuel cell system, overcoming the high cost, activity, and durability issues.

Keywords: oxygen reduction reaction; nitrogen-doped reduced graphene oxide; palladium; ruthenium; electrocatalyst

Citation: Park, G.-R.; Jo, S.G.; Varyambath, A.; Kim, J.; Lee, J.W. Nitrogen-Doped Reduced Graphene Oxide Supported $Pd_{4.7}Ru$ Nanoparticles Electrocatalyst for Oxygen Reduction Reaction. *Nanomaterials* **2021**, *11*, 2727. https://doi.org/10.3390/nano11102727

Academic Editor: Adriano Sacco

Received: 15 September 2021
Accepted: 11 October 2021
Published: 15 October 2021

1. Introduction

As the demand for renewable energy technology increases for a zero-emission society, energy conversion and storage devices are actively being studied. Among them, the fuel cell is one of the promising energy systems due to H_2 fuel, which has high energy density. Additionally, it emits only water as a by-product, without any pollutants such as carbon dioxide. Despite these advantages, it has a significant limitation: oxygen reduction reaction (ORR). ORR, the complex four electrons and multi-stepped reaction, works as the rate-determining step in fuel cells. For this reason, the use of catalysts is inevitable to facilitate the reaction of the cells. To date, carbon black supported Pt (Pt/CB) catalyst has been used the most widely due to its remarkable ORR performance. However, it has fatal disadvantages, including its high price, the scarcity of platinum, and the deterioration of carbon black under long operation periods. Therefore, innovative alternatives of Pt/CB with lower prices, abundance, and durability are essential for the development of renewable energy devices.

Regarding the active material, palladium has attracted attention as a promising ORR catalyst for its greater abundance than Pt and comparable properties, with the same crystal structure and group of the periodic table as Pt [1]. One of the efficient ways to improve its catalytic property and reduce its price is alloying Pd with other elements by rearranging the electronic structure, which is called the ensemble effect [2]. Among many metal elements,

Ru, which has also been considered as an efficient ORR catalyst, is located left of Pd in the periodic table and has some free states around the Pd Fermi level, thus facilitating the formation of alloys with the Pd [3,4]. Moreover, it also has advantages from the viewpoint of reserve and cost. Consequently, it is expected to have enhanced catalytic and economic benefits by alloying Pd with Ru.

Graphene, the two-dimensional carbon allotrope, has emerged as an efficient catalyst supporting material due to its high electrical conductivity, specific surface area, and physicochemical stability [5]. Reduced graphene oxide (rGO), synthesized through the oxidation-reduction process of graphite for graphene, is also a prominent carbon material with its high graphitization and intrinsic defects for particle anchoring sites [6]. According to prior research, it is known that doped nitrogen atoms in carbon lattice, especially the pyridinic N, work as efficient and stable particle anchoring sites by lone pair electrons, leading to preventing the activity deterioration by particle aggregation [7,8]. In addition, the nitrogen alters the geometry of the graphene plane with higher electronegativity by redistribution of the electronic density of the adjacent carbon atoms [9]. Also, the nitrogen is a conductive n-dopant with an extra valence electron than carbon, pushing the Fermi lever closer to the conduction band [10,11]. Furthermore, it improves O_2 adsorption, as the carbon atoms neighboring pyridinic N sites act as Lewis bases [12–14]. Therefore, the nitrogen-doped reduced graphene oxide (NrGO) is expected to have favorable material properties as a remarkable ORR catalyst support.

Herein, we fabricated NrGO supported Pd–Ru nanoparticles (NPs) catalysts. The NrGO was synthesized by thermal annealing using NH_3 flow, resulting in pyridinic N-dominant phase. After that, Pd-Ru NPs were decorated on the NrGO in a few nanometer size, uniformly by a facile solvothermal method [15]. The optimal ratio of metal contents for the best ORR performance was identified as 4.7:1 of Pd and Ru with 4.1 wt % of loading amount. So, the catalyst was labeled $Pd_{4.7}Ru$ NPs/NrGO. Due to the effects of nitrogen doping and well-dispersed NPs on the NrGO, $Pd_{4.7}Ru$ NPs/NrGO exhibited high electronic conductivity and electrochemical surface area (ECSA), leading to prior ORR performance. Furthermore, the $Pd_{4.7}Ru$ NPs/NrGO maintained its performance after 1000 cycles of a redox reaction, and even over 15 h of potentiostatic analysis without severe aggregation, proving its outstanding durability.

2. Materials and Methods

2.1. Synthesis of NrGO and rGO

NrGO was synthesized by doping nitrogen atoms to graphene oxide (GO, Global Graphene Group Inc., Dayton, OH, USA) sheets using a tube furnace. First, 100 mg of GO in an alumina boat was heated to 900 °C at a rate of 20 °C /min and maintained for 2 h under Ar/NH_3 atmosphere with a flow rate of 100/80 sccm in ambient pressure. To compare the effect of nitrogen incorporation in the graphene lattice, rGO was synthesized under the same process, except for NH_3 gas flow.

2.2. Synthesis of Pd–Ru NPs on NrGO and rGO

Pd–Ru NPs/NrGO catalysts were synthesized by a microwave-assisted method [16–18]. First, 55 mg of NrGO was dispersed in 50 mL of diethylene glycol (DEG, Junsei Chemical Co., Tokyo, Japan) by ultrasonication for 3 h. After that, 0.1 M palladium (II) chloride ($PdCl_2$, Wako Chemical Inc., Osaka, Japan) and ruthenium (III) chloride hydrate ($RuCl_3{\cdot}6H_2O$, Sigma-Aldrich Co., Burlington, MA, USA) were added into the solutions, totaling 1 mL in various ratios of 1:0, 4:1, 3:1, 1:1, and 0:1, respectively, to compare the catalytic activity depending on the elemental composition of Pd and Ru. At the same time, 1 mL of 0.5 M sodium hydroxide (NaOH, Junsei Chemical Co., Tokyo, Japan) was added to control reaction kinetics. Subsequently, the solutions were mixed by ultrasonication for another 1 h. After that, the prepared solutions were heated in a microwave oven at 700 W for 80 s. After cooling it to room temperature, DEG was separated by centrifugation at 8000 rpm for 50 min. Then, the catalysts were rinsed twice with acetone to remove residual DEG and impurities.

As a final step, the catalysts were dried in a vacuum oven at 60 °C overnight. Each catalyst was labeled as Pd NPs/NrGO, $Pd_{7.0}$Ru NPs/NrGO, $Pd_{4.7}$Ru NPs/NrGO, $Pd_{1.8}$Ru NPs/NrGO, and Ru NPs/NrGO, respectively, according to an inductively coupled plasma optic emission spectrometer (ICP-OES), as in Table S1. Moreover, the same procedures were applied to Pd–Ru NPs/rGO catalysts, labeled Pd NPs/rGO, $Pd_{6.7}$Ru NPs/rGO, $Pd_{4.5}$Ru NPs/rGO, $Pd_{1.3}$Ru NPs/rGO, and Ru NPs/rGO, respectively. Pt/CB (20 wt %, Alfa aesar., Haverhill, MA, USA) was used as a control sample without further purification.

2.3. Materials Characterization

The surface morphologies of the fabricated catalysts were characterized by transmission electron microscopy (FE-TEM, Talos F200X, Thermo Fisher Scientific, Waltham, MA, USA and Cs-corrected STEM, JEM-ARM200F, JEOL, Tokyo, Japan) equipped with energy dispersive X-ray spectroscopy (EDS, Talos F200X, Thermo Fisher Scientific, Waltham, MA, USA). The crystalline structures were determined with selected area diffraction (SAED) and X-ray diffraction (XRD, Xpert 3, Malvern Panalytical, Malvern, UK, Cu Kα anode). The chemical states and bonding characteristics were analyzed through X-ray photoelectron spectrometer (XPS, K-alpha System, Thermo Fisher Scientifics, Waltham, MA, USA) with a monochromatic Al Kα (1486.6 eV). Raman spectroscopy (Micro Raman Spectrometer, NRS-5100, JASCO International Co., Tokyo, Japan) with laser excitation line of 512 nm was used to analyze defective and graphitic structures of the NrGO and rGO based catalysts. Elemental compositions and contents of Pd and Ru were investigated by ICP-OES (Optima 8300, PerkinElmer, Waltham, MA, USA).

2.4. Electrochemical Measurements

All electrochemical measurements were conducted using a standard three-electrode cell system connected to an electrochemical workstation (VSP, Biologic, Knoxville, Tennessee, USA) with a rotating ring-disk electrode rotator (RRDE-3A, ALS, Tokyo, Japan) in 0.1 M KOH (85%, Junsei Chemical Co., Tokyo, Japan) electrolyte. Pt coil (EC Frontier, Kyoto, Japan) and Hg/HgO (saturated 20% KOH) were used as a counter electrode and a reference electrode, respectively. Catalyst ink was prepared by adding 3 mg of the prepared catalyst powder into 1 mL of isopropyl alcohol (IPA, OCI Co., Seoul, Korea) and 0.1 mL of Nafion solution (5 wt %, Alfa aesar., Haverhill, MA, USA), followed by dispersing with ultrasonication. After that, 20 μL of the catalyst ink was deposited on the glassy carbon working electrode (GCE, 5 mm diameter, ALS, Tokyo, Japan) with ~0.278 mg/cm^2 of loading mass and dried in the air.

ORR activities were estimated by linear sweep voltammetry (LSV). LSV measurements were carried out before and after the accelerated degradation test (ADT) by rotating the working electrode at 1600 rpm in an O_2-saturated electrolyte at 1 mV/s scan rate from 1.2 V_{RHE} to 0 V_{RHE}. To characterize the long-term durability of the catalysts with ADT, cyclic voltammetry (CV) was carried out for 1000 cycles at 50 mV/s scan rate from 1.2 V_{RHE} to 0 V_{RHE}. Additionally, electrochemical impedance spectroscopy (EIS) measurements were conducted before and after the ADT with a frequency range from 100 kHz to 100 mHz at 0.3 V_{RHE}. Chrono-amperometry (CA) measurements were carried out for 15 h at 0.3 V_{RHE} and 0.75 V_{RHE} with rotating the working electrode. ECSA was compared by calculating electrochemical double-layer capacitance (C_{dl}) from CV tests at scan rates with 5, 10, 25, 50, 100, 150, and 200 mV/s between 1.1 and 1.0 V_{RHE}. In addition, methanol and CO poisoning tests were conducted. For the methanol poisoning test, LSV curves were collected under the same conditions after dropping 1 mL of 1 M CH_3OH from 1.2 V_{RHE} to 0 V_{RHE} 1 mV/s of scan rate. In case of CO poisoning test, 5 cycles of CV under CO saturation at 50 mV/s scan rate and following LSV tests under O_2 saturation at 1 mV/s scan rate were carried out to estimate the CO poisoning at the same scan range. All measured potential values of V vs. Hg/HgO were calibrated to the reversible hydrogen electrode (RHE) scale by Equation (1), and the pH of 0.1 M KOH electrolyte was 13.01.

$$E_{RHE} = E_{Hg/HgO} + 0.098 + 0.059\ pH \quad (1)$$

3. Results and Discussions

Figure 1 displays the $Pd_{4.7}Ru$ NPs/NrGO and ORR on the catalyst surface. During the thermal annealing with NH_3 flow, graphene oxide (GO) is reduced to be the rGO, and nitrogen atoms form covalent bondings with the carbon atoms in the graphene lattice. Several N sites, such as pyrrolic, graphitic, and pyridinic N, were fabricated, and $Pd_{4.7}Ru$ NPs were synthesized by the microwave-assisted method in a few nanometer size, especially anchored on the pyridinic N sites. These could facilitate the ORR activity of the catalyst due to the higher electron conductivity from heterogenous atoms and improved O_2 adsorption by the effect of C atoms neighboring pyridinic N sites [12,13]. Furthermore, strong bonding between the catalyst and N sites might prevent the NPs from agglomeration or dissolution from the surface. $Pd_{4.7}Ru$ NPs grow in a form of a Pd-based face-centered cubic (FCC) structure, and the lattice could be also distorted when Ru atoms are introduced, resulting in higher ORR activity than merely being in a single metal, and it was maximized when the ratio of Pd and Ru was 4.5:1–4.7:1.

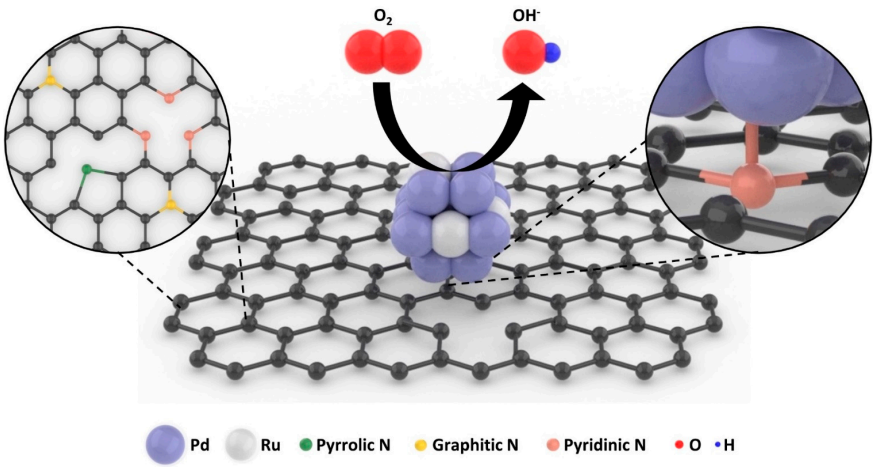

Figure 1. Schematic illustration of the $Pd_{4.7}Ru$ NPs/NrGO.

The surface morphologies of the $Pd_{4.7}Ru$ NPs/NrGO and $Pd_{4.5}Ru$ NPs/rGO were investigated by TEM analysis. $Pd_{4.7}Ru$ and $Pd_{4.5}Ru$ NPs are anchored on NrGO (Figure 2a) and rGO (Figure 2d), respectively, and both show the same d-spacing value of 0.22 nm, indicating a Pd (111) facet of FCC structure (see Figure 2b,e). Moreover, Figure 2a,d also show that $Pd_{4.7}Ru$ NPs were uniformly dispersed on the NrGO surface, whereas $Pd_{4.5}Ru$ NPs are partially aggregated on the rGO surface. Size distributions of the NPs, shown in Figure 2c,f, demonstrate that $Pd_{4.7}Ru$ NPs/NrGO has 2.4 nm on average, while $Pd_{4.5}Ru$ NPs/rGO presents 3.4 nm on average. The well-doped nitrogen acts as an efficient particle generation point and alleviates to form small and uniform particles with wide surface area, which might consequently improve catalytic reaction. Moreover, Figure S1a,c show that single Pd NPs on NrGO and rGO are shown agglomerated distribution, whereas single Ru NPs on the supports were dispersed in a sub-nanometer size, as shown in Figure S1b,d. These results suggest that the introduction of Ru in Pd lattice might affect the size and dispersity of NPs when synthesized.

To confirm the crystallinity of NPs, we collected selected area electron diffraction (SAED) patterns from the catalysts. The $Pd_{4.7}Ru$ NPs/NrGO is similar to Pd/NrGO, representing the rings of Pd (111), (200), (220), (311), and (331) planes (see Figure 2g and Figure S2a). Meanwhile, only Ru NPs/NrGO in Figure S2b shows Ru (101) and (200) facets, which could be distinguished from the abovementioned Pd planes. Additionally, the calculated Pd d-spacing value from the Pd (111) ring of the $Pd_{4.7}Ru$ NPs/NrGO (0.22 nm, shown in Table S2) was consistent with the value in Figure 2b. Interestingly, Table S2 represents that whole Pd d-spacing values for the $Pd_{4.7}Ru$ NPs/NrGO are smaller than the Pd NPs/NrGO. According to the interplanar spacing equation in cubic, $a = d/\sqrt{h^2 + k^2 + l^2}$, the lattice parameter a is proportional to the d. We calculated the corresponding values

from Pd (111) of the $Pd_{4.7}Ru$ NPs/NrGO and Pd NPs/rGO to compare the lattice size difference of $Pd_{4.7}Ru$ and Pd. After adding Ru in Pd lattice, the *d* value decreased from 0.23 nm to 0.22 nm, meaning a decrease in *a*, from 0.40 nm to 0.38 nm [19,20]. Regarding the $Pd_{4.7}Ru$ particles, when Ru atoms that have a smaller atomic radius than Pd are substituted in the Pd lattice, it might shrink the Pd lattice; this was confirmed by the decrease in d-spacing value. These results also support that Pd and Ru coexist as alloys, not as separate phases. For further characterization, we conducted mapping and line scanning elemental analyses by HAADF-EDS. Figure 2h demonstrates that N, Pd, and Ru are clearly detected. This demonstrates that Pd and Ru appear in the form of NPs on the N-doped graphene. Moreover, the line scanning image in Figure 2i shows that Pd and Ru are observed simultaneously, indicating that they coexist in the NP. Consequently, Pd and Ru are synthesized in a nanometer-size on the graphene lattice, forming the non-separated alloy structure.

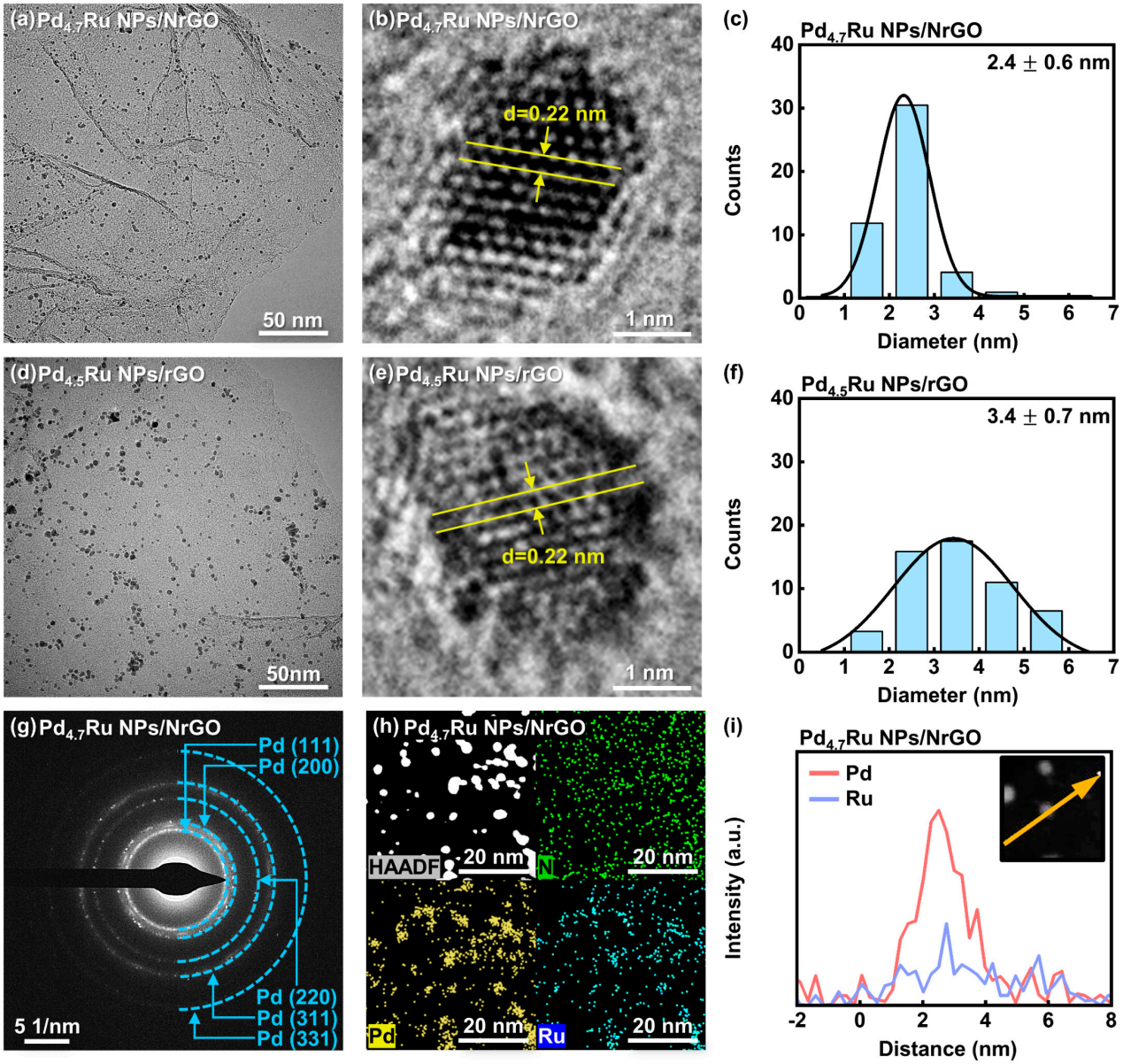

Figure 2. TEM and high-resolution image of the (**a**,**b**) $Pd_{4.7}Ru$ NPs/NrGO and (**d**,**e**) $Pd_{4.5}Ru$ NPs/rGO and the corresponding particle size distribution histograms of the (**c**) $Pd_{4.7}Ru$ NPs/NrGO and (**f**) $Pd_{4.5}Ru$ NPs/rGO. (**g**) SAED patterns of the $Pd_{4.7}Ru$ NPs/NrGO. (**h**) EDS mapping images and (**i**) line scanning of the $Pd_{4.7}Ru$ NPs/NrGO (Inset: HAADF images of the $Pd_{4.7}Ru$ NPs/NrGO in line scanning area).

Additional structural analyses for the NPs and the graphene-based supports were conducted by XRD and Raman spectroscopy. Figure 3a,b show the XRD patterns of the NrGO and rGO-based catalysts, respectively. All measured catalysts have common peaks around 25.0° from the graphite (002). However, there is no peak corresponding to either Pd or Ru in the Pd–Ru alloy and Ru-based catalysts. It is attributed to the result that small particles under 4 nm are anchored uniformly on the graphene-based supports, which is identical to the TEM results in Figure 2a,d and Figure S1b,d [21]. On the other hand, only Pd NPs both on the NrGO and rGO showed aggregated shapes and sized over 5 nm, as shown in Figure S2a,c, thus displaying a distinct peak at 40.4° in the XRD spectra. As it corresponds to FCC Pd (111) peak, we could confirm the FCC crystallinity of Pd along with the SAED patterns in Figure S2a.

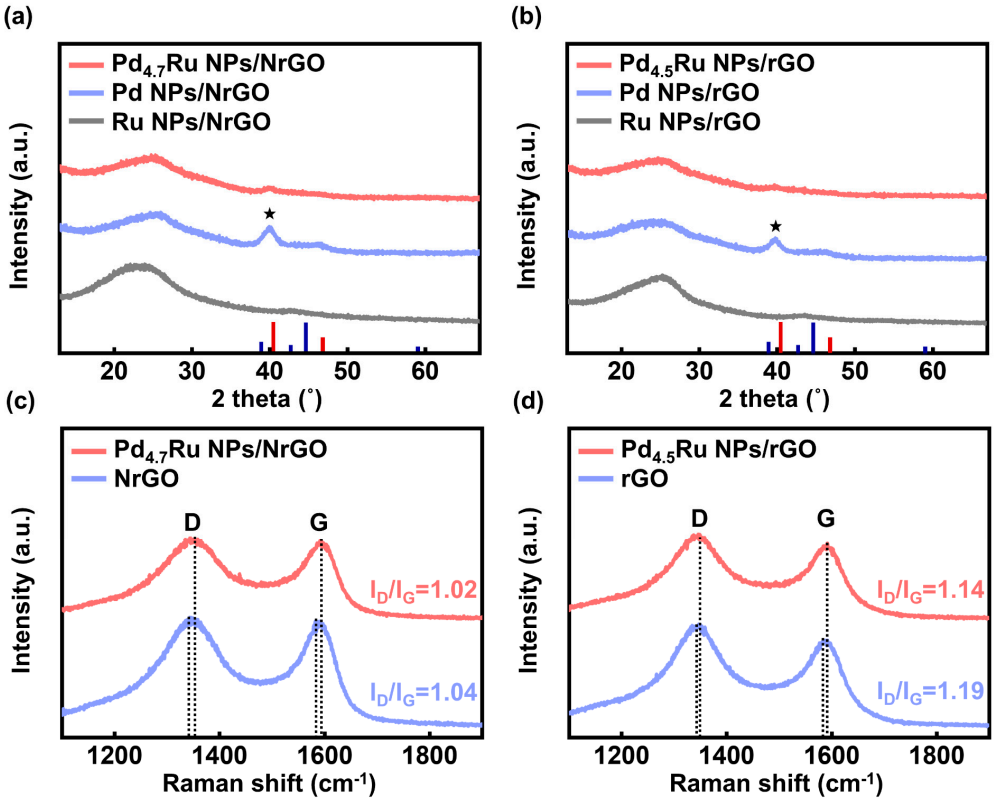

Figure 3. XRD patterns of (**a**) $Pd_{4.7}Ru$ NPs/NrGO, Pd NPs/NrGO, Ru NPs/NrGO and (**b**) $Pd_{4.5}Ru$ NPs/rGO, Pd NPs/rGO, Ru NPs/rGO. Red and blue bars indicate the peaks in the standard patterns of Pd (ICDD 00-001-1201) and Ru (ICDD 00-001-1253), respectively, and the stars correspond to Pd (111). Raman spectra of (**c**) $Pd_{4.7}Ru$ NPs/NrGO, NrGO and (**d**) $Pd_{4.5}Ru$ NPs/rGO, rGO, and the dotted line represents the Raman shift of D and G bands for each sample.

To compare the status of two graphene supports, we additionally conducted Raman spectroscopy. As shown in Figure 3c,d, all samples have two separate peaks around 1345 and 1590 cm^{-1} (Table 1) of the D and G bands, which contain the information of defects and graphitic degree [22,23]. The NrGO has a lower I_D/I_G ratio (1.04) than the rGO (1.19), indicating the ordered graphene system by the introduced nitrogen atoms [24,25]. Additionally, this tendency is consistent with Pd–Ru-anchored catalysts with values of 1.02 and 1.14 for the $Pd_{4.7}Ru$ NPs/NrGO and $Pd_{4.5}Ru$ NPs/rGO, respectively. Furthermore, blue-shifts of the D and G bands are observed in Pd–Ru NPs samples both on the NrGO and rGO, compared with the pristine NrGO and rGO sheets due to the compressive strain by anchoring particles [26,27]. Moreover, in the case of NrGO-based catalysts, the degree of the shifted D and G band is higher than the rGO-based catalyst, indicating that more compressive strain is applied over the NrGO after particle anchoring. It might connect to

the stronger bonding of $Pd_{4.7}Ru$ particles and NrGO than $Pd_{4.5}Ru$ and rGO as scattered at higher frequency.

Table 1. Raman shift values of the $Pd_{4.7}Ru$ NPs/NrGO, $Pd_{4.5}Ru$ NPs/rGO, NrGO, and rGO.

Sample	Raman Shift (cm^{-1})	
	D Band	G Band
$Pd_{4.7}Ru$ NPs/NrGO	1349.7	1591.6
$Pd_{4.5}Ru$ NPs/rGO	1346.2	1591.7
NrGO	1343.6	1588.3
rGO	1343.4	1588.7

We conducted XPS analyses to characterize the chemical states and bonding configurations of $Pd_{4.7}Ru$ NPs/NrGO and $Pd_{4.5}Ru$ NPs/rGO. In Figure 4a of C 1s spectra, common peaks at 284.7, 286.3, and 289.1 eV are observed from both samples, which corresponds to C–C, C–O, and C=O bonding, respectively [28,29]. C–C bonding originated from the graphene lattice, and C–O and C=O bondings are from the residual hydroxyl, carbonyl, and epoxy on the NrGO and rGO surfaces. In addition, only in the $Pd_{4.7}Ru$ NPs/NrGO sample, C–N bonding appears at 285.8 eV, indicating doped N atoms form stable covalent bonding with the neighboring C atoms. To clarify the bonding states of N atoms, N 1s spectra were also recorded at Figure 4b. The spectra are deconvoluted into pyridinic, pyrrolic, graphitic, and oxidized N peaks at 398.7, 399.8, 401.2, and 402.5 eV with ratios of 36.5, 31.9, 17.7, and 13.9%, respectively [30]. Previous research demonstrated that doped nitrogen atoms in carbon-based support, especially the pyridinic N, supply the particle anchoring sites, and the pyridinic N is dominant in this sample with the contents of 36.5% [7,8,18,31]. Likewise, it was proved in this research by comparing the N 1s peak of $Pd_{4.7}Ru$ NPs/NrGO and NrGO in Figure S3a. The pyridinic N peak in NrGO is displayed at 398.2 eV and shifted to 398.7 eV after synthesizing with $Pd_{4.7}Ru$ NPs, and it could be inferred as the NPs were anchored on pyridinic N [8,32]. Pd 3p photoemission lines in Figure 4c display two distinct peaks at 335.7 and 340.9 eV, corresponding with the metallic Pd $3d_{5/2}$ and Pd $3d_{3/2}$, respectively. Additionally, two oxidic states are shown simultaneously at 337.4 eV and 342.5 eV, which are matched with the Pd^{2+} $3d_{5/2}$ and Pd^{2+} $3d_{3/2}$, respectively. These peaks are detected at the same position in the Pd NPs/NrGO and Pd NPs/rGO, as shown in Figure S3b. Interestingly, Ru 3p spectra show only metallic peaks of Ru $3p_{1/2}$ and Ru $3p_{3/2}$ without any oxidized peak in the Pd–Ru-based catalysts (see Figure 4d), whereas both metallic and oxidic states are seen in Ru NPs (see Figure S3c). It is considered that the residual oxygen at graphene sheets might be reacted with Pd^{2+} ions preferentially than Ru^{4+} because it is reported that PdO is formed at lower temperature than RuO_2 [33–35]. From these results, we could assume that the $Pd_{4.7}Ru$ NPs/NrGO and the $Pd_{4.5}Ru$ NPs/rGO catalysts have metal-dominant phases of Pd and Ru.

To investigate electrochemical performance of the catalysts, we carried out the ORR analyses of the $Pd_{4.7}Ru$ NPs/NrGO, $Pd_{4.5}Ru$ NPs/rGO, and Pt/CB with a three-electrode system in O_2 gas saturated 0.1 M KOH electrolyte. Figure 5a shows the LSV measurement of cathodic scanning plots. Among the catalysts, the $Pd_{4.7}Ru$ NPs/NrGO achieves the highest onset potential at -0.1 mA/cm^2 and half-wave potential with 0.913 V_{RHE} and 0.792 V_{RHE}, followed by the Pt/CB with 0.908 V_{RHE} and 0.785 V_{RHE}, and $Pd_{4.5}Ru$ NPs/rGO with 0.863 V_{RHE} and 0.713 V_{RHE}, respectively (see Table 2). Additionally, the $Pd_{4.7}Ru$ NPs/NrGO, $Pd_{4.5}Ru$ NPs/rGO, and Pt/CB exhibited the limited current density of -6.33 mA/cm^2, -5.46 mA/cm^2, and -5.36 mA/cm^2 at 0.3 $V_{RHE,}$ and the specific activities were also plotted at Figure 5b. These results could be explained by the previous XPS analyses that doped pyridinic nitrogen atoms contribute to increasing the onset potential value of ORR. Additionally, we compared the activity of $Pd_{4.7}Ru$ NPs/NrGO to other previously studied Pd-based catalysts on their onset potential values, which are summarized in Table S3. Among them, nitrogen-doped carbon-supported Pd catalysts show relatively high onset potentials over 0.89 V_{RHE} than undoped catalysts, and it is explained by the

role of pyridinic N [36]. Moreover, the $Pd_{4.7}Ru$ catalyst has superior activity to Pd single element catalysts, confirming the alloying effect. We also compared the charge transfer resistance of the catalysts by EIS at 0.3 V_{RHE}. As represented in Figure 5c, three components constitute the Randles circuit: solution resistance R_s, charge transfer resistance R_{ct}, and C_{dl} [37]. R_s and R_{ct} were measured at 100 kHz and 100 mHz, respectively, and C_{dl} is shown in form of a semicircle as the frequency decreased. In the graph, the $Pd_{4.7}Ru$ NPs/NrGO has the lowest charge transfer value, of which R_{ct} is 115.2 Ω, followed by the $Pd_{4.5}Ru$ NPs/rGO and Pt/CB with 327.7 Ω and 336.7 Ω, respectively. This result confirms the higher conductivity of NrGO with more valence electrons of nitrogen atoms in honeycomb structure with carbon atoms. Additionally, it is consistent with the former results that oxygen reduction occurs faster on the $Pd_{4.7}Ru$ NPs/NrGO than commercial Pt/CB and $Pd_{4.5}Ru$ NPs/rGO. Additionally, to investigate the ORR activity according to the ratio of Pd and Ru, we carried out the LSV analyses on the prepared Pd–Ru alloy catalysts. LSV curves of the catalysts supported on the NrGO (Figure S4a) and rGO (Figure S4c) are exhibited, and Figure S4b,d show the corresponding specific activity at 0.3 V_{RHE}. Regardless of the supports, the histograms show the optimal value that $Pd_{4.7}Ru$ NPs/NrGO and $Pd_{4.5}Ru$ NPs/rGO have the highest current density in each case. Moreover, compared to the catalysts with similar Pd–Ru ratios on the NrGO and rGO, all NrGO-based catalysts show higher specific activity than the rGO-based ones.

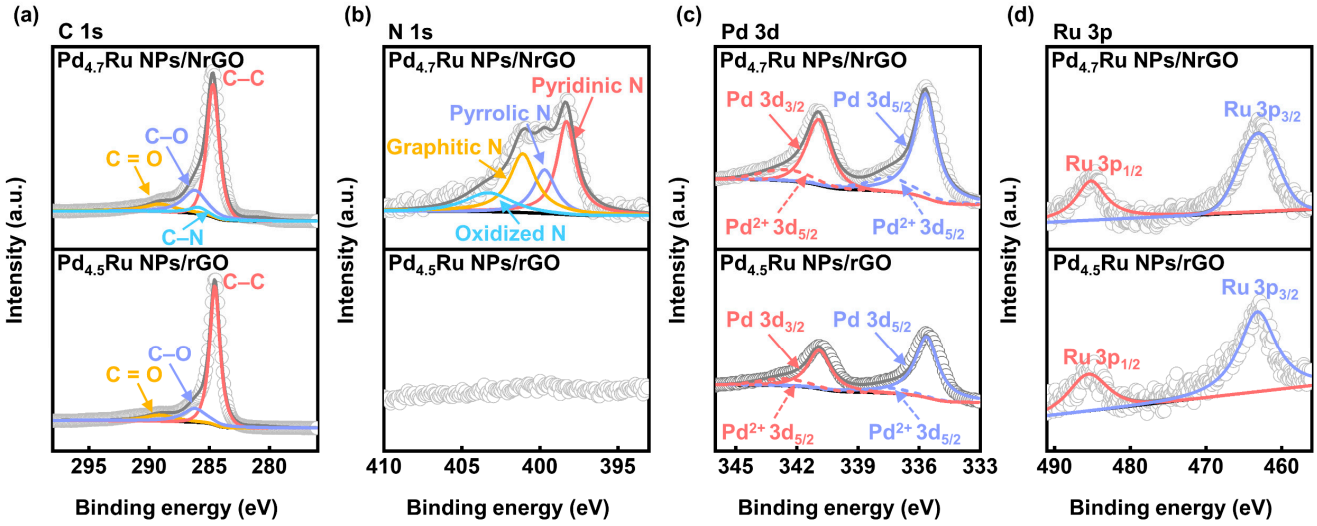

Figure 4. XPS spectra of (**a**) C 1s, (**b**) N 1s, (**c**) Pd 3d, and (**d**) Ru 3p of the $Pd_{4.7}Ru$ NPs/NrGO and $Pd_{4.5}Ru$ NPs/rGO.

Table 2. Onset potentials, half-wave potential, and current densities of the $Pd_{4.7}Ru$ NPs/NrGO, $Pd_{4.5}Ru$ NPs/rGO, and Pt/CB, determined from LSV at initial and after ADT. R_{ct} values of the $Pd_{4.7}Ru$ NPs/NrGO, $Pd_{4.5}Ru$ NPs/rGO, and Pt/CB, determined from EIS at initial and after CV ADT.

Sample	Onset Potential at −0.1 mA/cm² (V_{RHE})		Half-Wave Potential (V_{RHE})		Current Density at 0.3 V_{RHE} (mA/cm²)		R_{ct} (Ω)	
	Initial	After ADT	Initial	After ADT	Initial	After ADT	Initial	After ADT
$Pd_{4.7}Ru$ NPs/NrGO	0.913	0.870	0.792	0.760	−6.33	−6.30	115.2	119.2
$Pd_{4.5}Ru$ NPs/rGO	0.863	0.787	0.713	0.694	−5.46	−4.49	327.7	2063.0
Pt/CB	0.908	0.877	0.785	0.775	−5.36	−4.87	283.8	428.5

Additionally, we carried out the CV analyses at various scan rates with 5, 10, 25, 50, 100, 150, and 200 mV/s in the potential window between 1.10 V_{RHE} and 1.00 V_{RHE} to identify the ECSA of the catalysts. It could be calculated from the C_{dl} according to the equation: ECSA = C_{dl}/C_s. Thus, the ECSA is proportional to the C_{dl}, as the specific capacitance of a flat surface (C_s) is a constant value [38,39]. We plotted the difference of current densities

$|j_a - j_c|/2$ at 1.05 V_{RHE} against the scan rate, and the slope of the linear trend was C_{dl} [40]. Figure S5a–c exhibits the CV curves of the $Pd_{4.7}Ru$ NPs/NrGO, $Pd_{4.5}Ru$ NPs/rGO, and Pt/CB, respectively. We plotted the calculated $|ja - jc|/2$ and C_{dl} at Figure S5d and compared the ECSA of the catalysts. It is found that the $Pd_{4.7}Ru$ NPs/NrGO has the highest C_{dl} and ECSA, attributed to the well-dispersed NPs on graphene support, which was shown in the TEM images and corresponding size distribution histograms. This tendency is also coincident with the aforementioned LSV and EIS results, supporting the large active surface area of the $Pd_{4.7}Ru$ NPs/NrGO for promoting the electrocatalytic reaction.

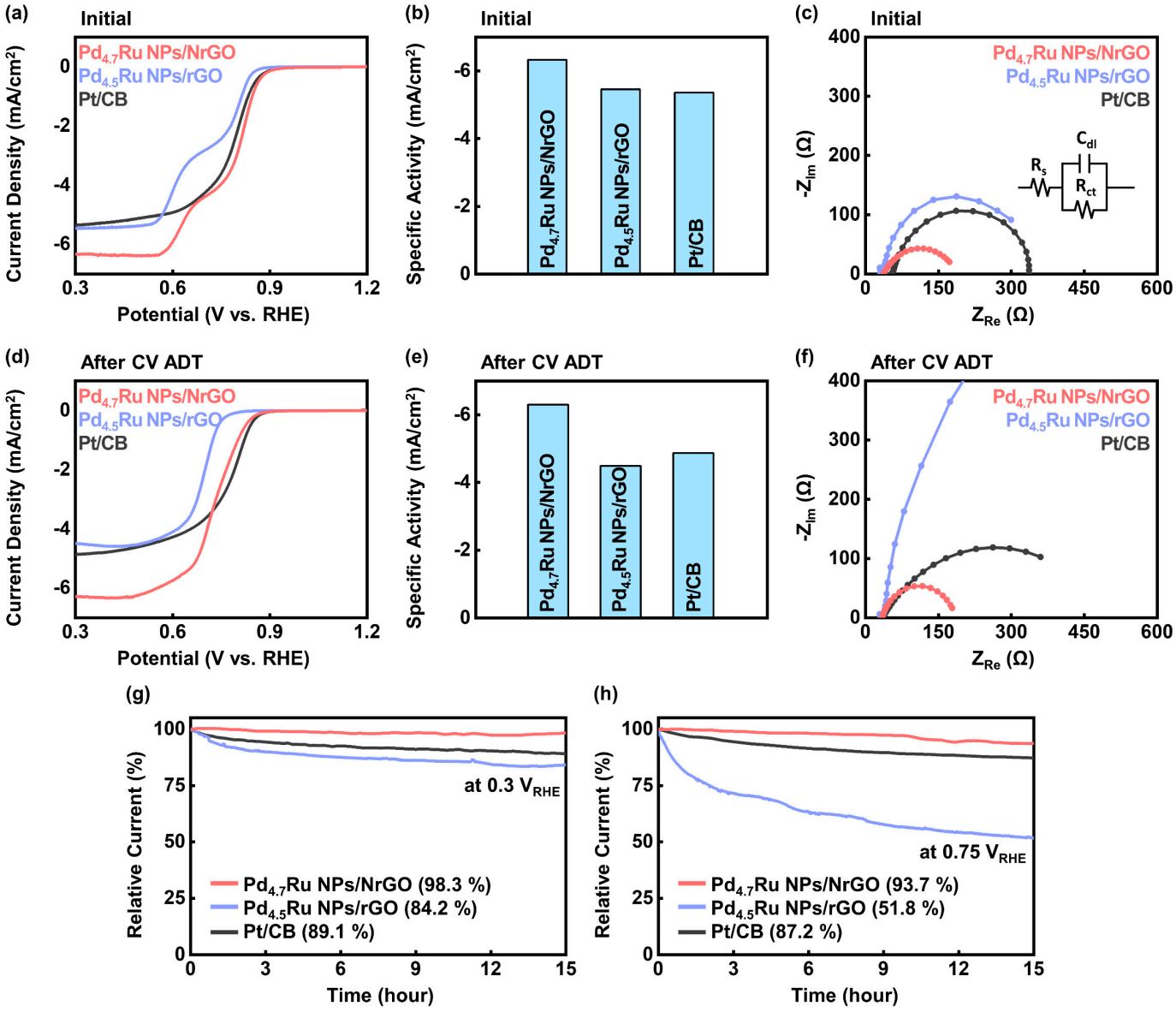

Figure 5. Electrochemical measurement for ORR. LSV curves of the (**a**) initial and (**d**) after CV ADT of the $Pd_{4.7}Ru$ NPs/NrGO, $Pd_{4.5}Ru$ NPs /rGO and corresponding (**b**,**e**) specific activities at 0.3 V_{RHE}. EIS curves of the (**c**) initial and (**f**) after CV ADT of the $Pd_{4.7}Ru$ NPs/NrGO, $Pd_{4.5}Ru$ NPs/rGO, and Pt/CB at the potential of 0.3 V_{RHE}. CA curves of the $Pd_{4.7}Ru$ NPs/NrGO, $Pd_{4.5}Ru$ NPs/rGO, and Pt/CB at (**g**) 0.3 V_{RHE} and (**h**) 0.75 V_{RHE}.

To observe the durability of the catalyst, we conducted an ADT by repeating CV for 1000 cycles from 0 V_{RHE} to 1.2 V_{RHE} at a scan rate of 50 mV/s. Figure 5d,e represent the LSV plots and corresponding specific activity histograms of the $Pd_{4.7}Ru$ NPs/NrGO, $Pd_{4.5}Ru$ NPs/rGO, and Pt/CB after ADT. The onset potential was shifted −43 mV and −76 mV for the $Pd_{4.7}Ru$ NPs/NrGO and $Pd_{4.5}Ru$ NPs/rGO, respectively, also achieving −6.30 mA/cm^2

and -4.49 mA/cm^2 at 0.3 V_{RHE}. Furthermore, EIS results in Figure 5f, also demonstrate that R_{ct} of the $Pd_{4.7}Ru$ NPs/NrGO was barely increased (119.2 Ω), whereas the resistance of the $Pd_{4.5}Ru$ NPs/rGO and Pt/CB were increased around 6.3 times (2063.0 Ω) and 1.5 times (428.5 Ω), respectively. In conclusion, the incorporation of N atoms in graphene lattice could facilitate enhanced catalytic activity during its repeated redox reaction for a long time.

To confirm the stability of the catalysts under the constant potential, we conducted a CA test at the saturated current potential with 0.3 V_{RHE} and the initiation potential of ORR with 0.75 V_{RHE} for 15 h. In Figure 5g,h, the NrGO-based catalysts show the retention of 98.3% and 93.7%, which are the highest values among all catalysts, whereas the rGO-based catalysts have the lowest value of the retention with 84.2% at 0.3 V_{RHE} and 51.8% at 0.75 V_{RHE}. These results are consistent with the abovementioned CV and EIS graphs and support our opinion that nitrogen introduction can affect the enhancement of catalytic durability. After the durability tests, the surface morphologies of the Pd–Ru alloy catalysts were observed by TEM. As shown in Figure S6a, the $Pd_{4.7}Ru$ particles are somewhat aggregated on the NrGO sheet, whereas the cohesive image of the $Pd_{4.5}Ru$ particles on the rGO sheet is clearly visible in Figure S6d. After, CA at 0.3 V_{RHE} (Figure S6b,e) and 0.75 V_{RHE} (Figure S6c,f) also appear the same tendency, indicating that the catalysts deteriorate their initial shape and distribution more during the reaction when supported on rGO than NrGO. Furthermore, we plotted the LSV graphs of the $Pd_{4.7}Ru$ NPs/NrGO, $Pd_{4.5}Ru$ NPs/rGO, and Pt/CB at Figure S7a–c, respectively, which were conducted under a CH_3OH and CO atmosphere to estimate their methanol tolerance and CO poisoning. The results confirm stability of the $Pd_{4.7}Ru$ NPs/NrGO, showing high retention of its current even under harsh condition, although the current of Pt/CB is decreased.

In general, we confirmed that the $Pd_{4.7}Ru$ NPs/NrGO catalyst exhibited prior catalytic performance in ORR to $Pd_{4.5}Ru$ NPs/rGO and even Pt/CB, the commercial catalyst. When we compare the performance of the NrGO and rGO-based catalysts intuitively, the result could be explained with the previous XPS analyses that the carbon atoms bonding with dominant pyridinic N are active sites for O_2 adsorption, and they contribute to the high onset potential of ORR by acting as Lewis bases [12,13]. In addition, the N atoms, which have a different number of valence electrons from C, could promote faster electronic conduction and the EIS data supports this effect. Moreover, the well-distributed, small-size particles of the $Pd_{4.7}Ru$ NPs/NrGO make their active area broader, generating high current density, and it was proven by the ECSA results. The particles, grown on N anchoring sites, have strong bondings with the carbon support, preventing aggregation during the reaction.

4. Conclusions

We fabricated $Pd_{4.7}Ru$ NPs decorated catalysts supported by NrGO and characterized them with a series of analytical methods. The NrGO was fabricated by thermal annealing of the GO in Ar/NH_3 atmospheres, followed by anchoring 4.1 wt % of $Pd_{4.7}Ru$ NPs on the carbon supports with the microwave-assisted method. XPS results displayed pyridinic, graphitic, pyrrolic, and oxidized N, which are doped on graphene sheets, and among them, the pyridinic N exists abundantly, with 36.5% contents in the $Pd_{4.7}Ru$ NPs/NrGO catalyst. It facilitates the ORR because the C atoms, bonding with pyridinic N, act as active O_2 adsorption sites. Additionally, doped nitrogen atoms contributed to well-dispersed $Pd_{4.7}Ru$ NPs with an average size of 2.4 nm on the NrGO, confirmed by TEM analysis, which might be attributed to its high ECSA. Moreover, the nitrogen atoms could transfer their valence electrons to the NPs. It could decrease charge transfer resistance on the catalyst surface and improve conductivity confirmed from EIS results. These factors promoted the ORR activity in the electrochemical test, showing higher limited current density, onset potential, half-wave potential, and lower charge transfer resistance than the $Pd_{4.5}Ru$ NPs/rGO and commercial Pt/CB with the value of -6.33 mA/cm^2, 0.913 V_{RHE}, 0.792 V_{RHE}, and 115.2 Ω, respectively. Moreover, the $Pd_{4.7}Ru$ NPs/NrGO catalyst showed the highest retention among all measured catalysts with 98.3% at 0.3 V_{RHE} and 93.3% at 0.75 V_{RHE}. Furthermore, it maintained initial morphology even after 1000 cycles of CV

ADT and 15 h of CA durability test. Consequently, we demonstrated that the NrGO is remarkable carbon-based support with the $Pd_{4.7}Ru$ NPs for durable and low costed ORR catalysts as a promising alternative of the Pt/CB.

Supplementary Materials: The following are available online at https://www.mdpi.com/article/10.3390/nano11102727/s1, Figure S1: TEM images of the (a) Pd NPs/NrGO, (b) Ru NPs/NrGO, (c) Pd NPs/rGO, and (d) Ru NPs/rGO. Figure S2: SAED patterns of the (a) Pd NPs/NrGO and (b) Ru NPs/NrGO. Figure S3: XPS survey spectra of (a) N 1s of the $Pd_{4.7}Ru$ NPs/NrGO and NrGO with dotted line for shifts comparison of pyridinic N, pyrrolic N, and graphitic N, (b) Pd 3d of the Pd NPs/NrGO and Pd NPs/rGO, and (c) Ru 3p of the Ru NPs/NrGO, Ru NPs/rGO. Figure S4: LSV curves of the (a) Pd–Ru NPs/NrGO catalysts, (c) Pd–Ru NPs/rGO catalysts and (b), (d) their corresponding specific activities at 0.3 V_{RHE}. Figure S5: CV curves of the (a) $Pd_{4.7}Ru$ NPs/NrGO, (b) $Pd_{4.5}Ru$ NPs/rGO and (c) Pt/CB between 1.00 and 1.10 V_{RHE} at different scan rates of 5, 10, 25, 50, 100, 150 and 200 mV/s. (d) Linear fittings of current densities at 1.05 V_{RHE} versus scan rates for the CV tests. Figure S6: TEM images of $Pd_{4.7}Ru$ NPs/NrGO after (a) 1000 cycles CV ADT, (b) CA at 0.3 V_{RHE}, (c) CA at 0.75 V_{RHE} and of $Pd_{4.5}Ru$ NPs/rGO after (a) 1000 cycles CV ADT, (b) CA at 0.3 V_{RHE}, (c) CA at 0.75 V_{RHE}. Figure S7: The response of (a) $Pd_{4.7}Ru$ NPs/NrGO, (b) $Pd_{4.5}Ru$ NPs/rGO, and (c) Pt/CB to CO saturation and 1 M CH_3OH in 0.1 M KOH. Table S1: Elemental contents and of the Pd–Ru NPs/NrGO and Pd–Ru NPs/rGO determined from ICP-OES. Table S2: D-spacing values of the $Pd_{4.7}Ru$ NPs/NrGO, Pd NPs/NrGO, and Ru NPs/NrGO calculated from SAED pattens. Table S3: Comparison of the onset potential of $Pd_{4.7}Ru$ NPs/NrGO with previously reported Pd and Ru catalysts towards ORR.

Author Contributions: Conceptualization, J.W.L.; data curation, experimental methodology, analysis, investigation, data visualization, manuscript writing, G.-R.P.; manuscript editing, S.G.J., J.K. and J.W.L.; review, S.G.J., A.V., J.K. and J.W.L.; funding acquisition, supervision, project administration, J.W.L. All authors have read and agreed to the published version of the manuscript.

Funding: This research was supported by Nano·Material Technology Development Program (2009-0082580) through National Research Foundation of Korea (NRF-2017M3A7B4049466, NRF-2020R1C1C1013900, No. 2021R1F1A1061304) that are funded by the Ministry of Science, ICT, and Future Planning.

Data Availability Statement: Data are contained within the article or Supplementary Materials.

Conflicts of Interest: The authors declare no conflict of interest.

References

1. Bhowmik, T.; Kundu, M.K.; Barman, S. Highly active and durable Pd nanoparticles-porous graphitic carbon nitride composite for electrocatalytic oxygen reduction reaction. *Int. J. Hydrogen Energy* **2016**, *41*, 14768–14777. [CrossRef]
2. Tian, J.; Wu, W.; Tang, Z.; Wu, Y.; Burns, R.; Tichnell, B.; Liu, Z.; Chen, S. Oxygen reduction reaction and hydrogen evolution reaction catalyzed by Pd–Ru nanoparticles encapsulated in porous carbon nanosheets. *Catalysts* **2018**, *8*, 329. [CrossRef]
3. Hubkowska, K.; Łukaszewski, M.; Czerwiński, A. Pd–Ru electrodeposits with high hydrogen absorption capacity. *Electrochem. Commun.* **2012**, *20*, 175–177. [CrossRef]
4. Xiao, M.; Gao, L.; Wang, Y.; Wang, X.; Zhu, J.; Jin, Z.; Liu, C.; Chen, H.; Li, G.; Ge, J. Engineering energy level of metal center: Ru single-atom site for efficient and durable oxygen reduction catalysis. *J. Am. Chem. Soc.* **2019**, *141*, 19800–19806. [CrossRef]
5. Julkapli, N.M.; Bagheri, S. Graphene supported heterogeneous catalysts: An overview. *Int. J. Hydrogen Energy* **2015**, *40*, 948–979. [CrossRef]
6. Xue, C.; An, H.; Yang, G. Facile construction of MoS2/CdS eutectic clusters anchored on rGO edge with enhanced hydrogen generation performance. *Catal. Today* **2018**, *317*, 99–107. [CrossRef]
7. Cui, X.L.; Long, Y.; Zhou, X.; Yu, G.Q.; Yang, J.; Yuan, M.; Ma, J.T.; Dong, Z.P. Pd-doped Ni nanoparticle-modified N-doped carbon nanocatalyst with high Pd atom utilization for the transfer hydrogenation of nitroarenes. *Green Chem.* **2018**, *20*, 1121–1130. [CrossRef]
8. Warczinski, L.; Hu, B.; Eckhard, T.; Peng, B.X.; Muhler, M.; Hattig, C. Anchoring of palladium nanoparticles on N-doped mesoporous carbon. *Phys. Chem. Chem. Phys.* **2020**, *22*, 21317–21325. [CrossRef]
9. Li, D.; Duan, X.; Sun, H.; Kang, J.; Zhang, H.; Tade, M.O.; Wang, S. Facile synthesis of nitrogen-doped graphene via low-temperature pyrolysis: The effects of precursors and annealing ambience on metal-free catalytic oxidation. *Carbon* **2017**, *115*, 649–658. [CrossRef]
10. Duan, J.; Chen, S.; Jaroniec, M.; Qiao, S.Z. Heteroatom-doped graphene-based materials for energy-relevant electrocatalytic processes. *Acs Catal.* **2015**, *5*, 5207–5234. [CrossRef]

11. Wu, G.; Santandreu, A.; Kellogg, W.; Gupta, S.; Ogoke, O.; Zhang, H.; Wang, H.-L.; Dai, L. Carbon nanocomposite catalysts for oxygen reduction and evolution reactions: From nitrogen doping to transition-metal addition. *Nano Energy* **2016**, *29*, 83–110. [CrossRef]
12. Guo, D.H.; Shibuya, R.; Akiba, C.; Saji, S.; Kondo, T.; Nakamura, J. Active sites of nitrogen-doped carbon materials for oxygen reduction reaction clarified using model catalysts. *Science* **2016**, *351*, 361–365. [CrossRef]
13. He, F.; Li, K.; Yin, C.; Wang, Y.; Tang, H.; Wu, Z.J. Single Pd atoms supported by graphitic carbon nitride, a potential oxygen reduction reaction catalyst from theoretical perspective. *Carbon* **2017**, *114*, 619–627. [CrossRef]
14. Xiang, Q.; Liu, Y.; Zou, X.; Hu, B.; Qiang, Y.; Yu, D.; Yin, W.; Chen, C. Hydrothermal synthesis of a new kind of N-doped graphene gel-like hybrid as an enhanced ORR electrocatalyst. *ACS Appl. Mater. Interfaces* **2018**, *10*, 10842–10850. [CrossRef]
15. Skorupska, M.; Ilnicka, A.; Lukaszewicz, J.P. N-doped graphene foam obtained by microwave-assisted exfoliation of graphite. *Sci. Rep.* **2021**, *11*, 1–11. [CrossRef]
16. Kim, J.; Kim, S.I.; Jo, S.G.; Hong, N.E.; Ye, B.; Lee, S.; Dow, H.S.; Lee, D.H.; Lee, J.W. Enhanced activity and durability of Pt nanoparticles supported on reduced graphene oxide for oxygen reduction catalysts of proton exchange membrane fuel cells. *Catal. Today* **2020**, *352*, 10–17. [CrossRef]
17. Lee, J.W.; Jeon, H.J.; Shin, H.-J.; Kang, J.K. Superparamagnetic Fe_3O_4 nanoparticles–carbon nitride nanotube hybrids for highly efficient peroxidase mimetic catalysts. *Chem. Commun.* **2012**, *48*, 422–424. [CrossRef]
18. Lee, J.W.; Jeong, H.M.; Lee, G.H.; Jung, Y.W.; Jo, S.G.; Kang, J.K. Agglomeration-Free Fe_3O_4 anchored via nitrogen mediation of carbon nanotubes for high-performance arsenic adsorption. *J. Environ. Chem. Eng.* **2021**, *9*, 104772. [CrossRef]
19. Escudero-Escribano, M.; Malacrida, P.; Hansen, M.H.; Vej-Hansen, U.G.; Velázquez-Palenzuela, A.; Tripkovic, V.; Schiøtz, J.; Rossmeisl, J.; Stephens, I.E.; Chorkendorff, I. Tuning the activity of Pt alloy electrocatalysts by means of the lanthanide contraction. *Science* **2016**, *352*, 73–76. [CrossRef]
20. Podjaski, F.; Weber, D.; Zhang, S.; Diehl, L.; Eger, R.; Duppel, V.; Alarcón-Lladó, E.; Richter, G.; Haase, F.; Fontcuberta i Morral, A.; et al. Rational strain engineering in delafossite oxides for highly efficient hydrogen evolution catalysis in acidic media. *Nat. Catal.* **2020**, *3*, 55–63. [CrossRef]
21. Tang, M.H.; Mao, S.J.; Li, M.M.; Wei, Z.Z.; Xu, F.; Li, H.R.; Wang, Y. RuPd Alloy Nanoparticles Supported on N-Doped Carbon as an Efficient and Stable Catalyst for Benzoic Acid Hydrogenation. *Acs Catal.* **2015**, *5*, 3100–3107. [CrossRef]
22. Ion-Ebrașu, D.; Andrei, R.D.; Enache, S.; Căprărescu, S.; Negrilă, C.C.; Jianu, C.; Enache, A.; Boerașu, I.; Carcadea, E.; Varlam, M. Nitrogen Functionalization of CVD Grown Three-Dimensional Graphene Foam for Hydrogen Evolution Reactions in Alkaline Media. *Materials* **2021**, *14*, 4952. [CrossRef]
23. Jiang, F.; Zhang, J.; Li, N.; Liu, C.; Zhou, Y.; Yu, X.; Sun, L.; Song, Y.; Zhang, S.; Wang, Z. Nitrogen-doped graphene prepared by thermal annealing of fluorinated graphene oxide as supercapacitor electrode. *J. Chem. Technol. Biotechnol.* **2019**, *94*, 3530–3537. [CrossRef]
24. Mu, X.W.; Yuan, B.H.; Feng, X.M.; Qiu, S.L.; Song, L.; Hu, Y. The effect of doped heteroatoms (nitrogen, boron, phosphorus) on inhibition thermal oxidation of reduced graphene oxide. *RSC Adv.* **2016**, *6*, 105021–105029. [CrossRef]
25. Vinod, K.R.; Saravanan, P.; Kumar, T.R.S.; Radha, R.; Balasubramaniam, M.; Balakumar, S. Enhanced shielding effectiveness in nanohybrids of graphene derivatives with Fe_3O_4 and epsilon-Fe_3N in the X-band microwave region. *Nanoscale* **2018**, *10*, 12018–12034. [CrossRef]
26. Mishra, A.; Singh, V.K.; Mohanty, T. Coexistence of interfacial stress and charge transfer in graphene oxide-based magnetic nanocomposites. *J. Mater. Sci.* **2017**, *52*, 7677–7687. [CrossRef]
27. Ni, Z.H.; Wang, Y.Y.; Yu, T.; Shen, Z.X. Raman Spectroscopy and Imaging of Graphene. *Nano Res.* **2008**, *1*, 273–291. [CrossRef]
28. Li, Z.Y.; Gao, Q.M.; Zhang, H.; Tian, W.Q.; Tan, Y.L.; Qian, W.W.; Liu, Z.P. Low content Pt nanoparticles anchored on N-doped reduced graphene oxide with high and stable electrocatalytic activity for oxygen reduction reaction. *Sci. Rep.* **2017**, *7*. [CrossRef] [PubMed]
29. Gautam, R.K.; Bhattacharjee, H.; Mohan, S.V.; Verma, A. Nitrogen doped graphene supported alpha-MnO_2 nanorods for efficient ORR in a microbial fuel cell. *RSC Adv.* **2016**, *6*, 110091–110101. [CrossRef]
30. Ma, J.W.; Habrioux, A.; Luo, Y.; Ramos-Sanchez, G.; Calvillo, L.; Granozzi, G.; Balbuena, P.B.; Alonso-Vante, N. Electronic interaction between platinum nanoparticles and nitrogen-doped reduced graphene oxide: Effect on the oxygen reduction reaction. *J. Mater. Chem. A* **2015**, *3*, 11891–11904. [CrossRef]
31. Lee, J.W.; Viswan, R.; Choi, Y.J.; Lee, Y.; Kim, S.Y.; Cho, J.; Jo, Y.; Kang, J.K. Facile Fabrication and Superparamagnetism of Silica-Shielded Magnetite Nanoparticles on Carbon Nitride Nanotubes. *Adv. Funct. Mater.* **2009**, *19*, 2213–2218. [CrossRef]
32. Peng, L.; Shang, Y.; Gao, B.; Xu, X. Co_3O_4 anchored in N, S heteroatom co-doped porous carbons for degradation of organic contaminant: Role of pyridinic N-Co binding and high tolerance of chloride. *Appl. Catal. B Environ.* **2021**, *282*, 119484. [CrossRef]
33. Lasch, K.; Jorissen, L.; Friedrich, K.A.; Garche, J. The function of ruthenium oxides in Pt-Ru catalysts for methanol electro-oxidation at low temperatures. *J. Solid State Electrochem.* **2003**, *7*, 619–625. [CrossRef]
34. Xiong, H.F.; Lester, K.; Ressler, T.; Schlogl, R.; Allard, L.F.; Datye, A. Metastable Pd <-> PdO Structures During High Temperature Methane Oxidation. *Catal. Lett.* **2017**, *147*, 1095–1103. [CrossRef]
35. Rahul, R.; Singh, R.K.; Bera, B.; Devivaraprasad, R.; Neergat, M. The role of surface oxygenated-species and adsorbed hydrogen in the oxygen reduction reaction (ORR) mechanism and product selectivity on Pd-based catalysts in acid media. *Phys. Chem. Chem. Phys.* **2015**, *17*, 15146–15155. [CrossRef] [PubMed]

36. Ejaz, A.; Jeon, S. The individual role of pyrrolic, pyridinic and graphitic nitrogen in the growth kinetics of Pd NPs on N-rGO followed by a comprehensive study on ORR. *Int. J. Hydrogen Energy* **2018**, *43*, 5690–5702. [CrossRef]
37. Bard, A.J.; Faulkner, L.R. Fundamentals and applications. *Electrochem. Methods* **2001**, *2*, 580–632.
38. Chai, L.L.; Zhang, L.J.; Wang, X.; Xu, L.Q.; Han, C.; Li, T.T.; Hu, Y.; Qian, J.J.; Huang, S.M. Bottom-up synthesis of MOF-derived hollow N-doped carbon materials for enhanced ORR performance. *Carbon* **2019**, *146*, 248–256. [CrossRef]
39. Kang, B.K.; Im, S.Y.; Lee, J.; Kwag, S.H.; Kwon, S.B.; Tiruneh, S.; Kim, M.J.; Kim, J.H.; Yang, W.S.; Lim, B.; et al. In-situ formation of MOF derived mesoporous Co_3N/amorphous N-doped carbon nanocubes as an efficient electrocatalytic oxygen evolution reaction. *Nano Res.* **2019**, *12*, 1605–1611. [CrossRef]
40. Bai, L.; Duan, Z.Y.; Wen, X.D.; Si, R.; Zhang, Q.Q.; Guan, J.Q. Highly Dispersed Ruthenium-Based Multifunctional Electrocatalyst. *ACS Catal.* **2019**, *9*, 9897–9904. [CrossRef]